
High-Resolution Neutron Imaging of Laser-Imploded DT Targets

Imaging the neutrons produced by implosions at the National Ignition Facility¹ or the Laser Mega Joule² will require spatial resolution as good as $5\ \mu\text{m}$ (Ref. 3) to identify failure mechanisms such as poor implosion symmetry or improper laser pulse shaping. An important step to achieving this goal is reported in this article. Neutron images were obtained from OMEGA implosions with both high resolution and narrow diameters that confirm the resolution and agree with calculations. Ress *et al.*⁴ obtained the first neutron images of ICF capsules with a geometric resolution of $80\ \mu\text{m}$ and a full width at half-maximum (FWHM) of $150\ \mu\text{m}$. Delage *et al.*⁵ reported geometrical resolution of $56\ \mu\text{m}$ and overall resolutions of 100 to $180\ \mu\text{m}$ with FWHM's of 150 to $250\ \mu\text{m}$. The measurements reported in this article [carried out on LLE's OMEGA laser by a team of scientists from Commissariat à l'Énergie Atomique (CEA), LLE, and LANL] achieved a geometrical resolution of $30\ \mu\text{m}$ and an overall resolution of $45\ \mu\text{m}$ with a FWHM of $62\ \mu\text{m}$.

Imaging neutrons at high resolution is a challenging task being carried out at several laboratories using pinhole⁶ or penumbral apertures. CEA's experimental system using the penumbral technique,⁷ as well as a new analytical approach for estimating the overall resolution, was successfully tested on OMEGA in a direct-drive experiment. The basis of the design is to use an aperture whose diameter is large compared to the size of the neutron source. The shape of the aperture is biconical and is optimized in order to amplify the penumbra of the source in the image plane. The aperture is larger than that for a pinhole, allowing easier fabrication and stronger signals, especially important when signal levels are low. An unfolding process is needed, however, to recover an image; this process includes low bandpass filtering, which affects the resolution. This article reviews the main mechanisms that limit the spatial resolution of a penumbral imaging system: the spatial resolution of the detector, the shape of the aperture, and the process of unfolding the image.

After propagating through the experimental chamber and target area and scattering from various experimental hardware

and structures, the 14-MeV neutrons arriving at the detector are spread in time and angle. Moreover, these neutrons create a large number of gamma rays in the 0- to 10-MeV range by (n, γ) reactions on the experimental hardware. The direct neutrons that form the image need to be discriminated from the scattered neutrons and the gamma rays. Bubble detectors⁸ can discriminate among gamma rays, low-energy neutrons, and 14-MeV neutrons. They offer potentially high spatial resolution, but their efficiency is still very low (1.4×10^{-5}) and they require a sophisticated readout system.

Plastic scintillators with response times of the order of 10 ns can discriminate particles by arrival time. The detector contains 8000 scintillating fibers, each with a length of 10 cm, a square section of $1.5\ \text{mm}^2$, and an e -fold decay time of 12 ns. The intrinsic detection efficiency ε is 27%. The sampling theorem limits the spatial resolution of the instrument to a geometrical resolution of $2\delta_{\text{pix}}/G$, where G is the magnification ratio of the system and δ_{pix} is the pixel size.

In a plastic scintillator, fast neutrons interact mainly by elastic scattering on hydrogen. The high-energy protons lose energy in the medium (calculated with the Birks model⁹) and produce light about the scattering point with a FWHM of $0.910\ \text{mm}$ (δ_{rec}).¹⁰ This limits the resolution of the system to δ_{rec}/G . This intrinsic limitation required a high magnification ratio to achieve a high-resolution design.

The image is relayed optically by a mirror and a lens from the detector onto a gated microchannel plate (MCP); the output image of the MCP is reduced by a fiber-optics taper and then recorded on a charge-coupled device (CCD) with a $19\text{-}\mu\text{m}$ pixel size. The CCD is shielded by a 25-cm-thick piece of plastic followed by 5 cm of lead. At 8 m from the source, the external dose of 12 mrad for a 10^{14} neutron yield is reduced to several mrad inside the shield (an upper acceptable limit for the CCD). The detector image size is reduced to 0.27 and 0.068 of its original dimension onto the MCP and the CCD, respectively. Each fiber of the detector is recorded on the average onto a 5-by-5 array of CCD pixels. The spatial resolution of the

MCP is $70 \mu\text{m}$ at FWHM, much smaller than the size of the detector pixel imaged onto the MCP ($405 \mu\text{m}$). We conclude that the spatial resolution of our recording system is negligible compared to the spatial resolution of the detector.

The point-spread function (PSF) of the aperture is the neutron intensity distribution in the image plane for an isotropic point source located in the middle of the field of view. For a given entrance hole diameter, this PSF depends only on the field of view and the distance from the source. Figure 86.32 shows dependence of the FWHM (δ_{bic}) of the PSF on the distance from the middle of the aperture to the target (L_0). Increasing the distance from the source to the aperture can improve the spatial resolution to less than $10 \mu\text{m}$. For these experiments, however, the magnification ratio decreases with L_0 because the distance between the source and the scintillator (L_i) is limited to 8 m. An optimal value for L_0 , including the resolution of the detector, is found to be 80 mm.

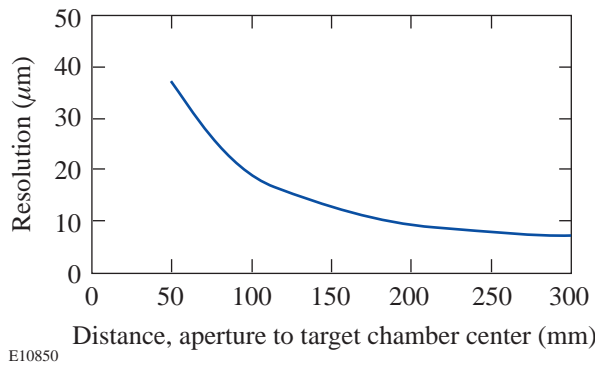


Figure 86.32

The spatial resolution limit (FWHM of the point-spread function) for the biconical aperture versus the distance (L_0) from its center to the source.

A hole was recently dug in the concrete floor of the OMEGA Target Bay to allow a 13-m line of sight. A new detector will be installed with $250\text{-}\mu\text{m}$ -diam capillaries filled with deuterated liquid scintillator. The new $250\text{-}\mu\text{m}$ pixel size and estimated δ_{rec} of $500 \mu\text{m}$ lead to a redesigned aperture placed at $L_0 = 160$ mm. These modifications should reduce the noise background by a factor of 100 and allow a $13\text{-}\mu\text{m}$ resolution.

Several methods exist to unfold penumbral images.¹¹ After testing these methods on synthetic penumbral images, the autocorrelation method¹² was found to give the best results with minimum mathematical complexity. Most penumbral unfolding processes assume that the aperture can be repre-

sented by a thin hole of radius R_d surrounded by a medium with a transmission τ to neutrons. With this assumption, the Fourier transform I of the image is the product of the Fourier transform S of the source and the aperture: $I(k) = S J_1(2\pi k R_d) / \pi k R_d$, where J_1 is the first-order Bessel function. The unfolding process consists of multiplying I by a function U , which has the following mathematical properties: inverse Fourier transform $[U J_1(2\pi k R_d) / \pi k R_d] = \delta$, the Dirac function, and a small amplitude oscillatory function at radius $2R_d$, which is outside the field of view. We find $U = 2J_1(2\pi k R_d) k^3 / \pi k R_d$. The multiplication of I by U gives the Fourier transform of the source image, avoiding any problems caused by dividing by zero.

In practice, the unfolded Fourier transform of the image contains both noise and the signal from the spatial distribution of the neutron source. The primary source of noise is the Poisson statistics of events in the detector. Reducing this noise requires a low band-pass filtration that limits overall design performance. A reliable criterion to find the frequency at which noise starts to dominate is to set the noise power spectrum equal to the power spectrum of the signal without noise.¹³

For Poisson noise, it can be shown that the power spectrum of the image with noise, P_{s+n} , is the sum of the power spectrum of the image without noise, P_s , and the spectrum N_s of the number of detected neutrons in the full field of the image.¹⁴ For an homogeneous neutron source of radius R_s and yield N , we have

$$N_s = \frac{\epsilon N G^2}{4(L_i + L_0)^2} \left[(1 - \tau) R_d^2 + \tau (R_d + R_s)^2 \right],$$

$$P_s = \left[\frac{\epsilon (1 - \tau) N R_d^2 G^2}{4(L_i + L_0)^2} \frac{J_1(2\pi k R_d)}{\pi k R_d} \frac{J_1(2\pi k R_s)}{\pi k R_s} \right]^2.$$

Using the first-order approximation of the Bessel function valid for $k R_{d,s}$ greater than about 1.2 (appropriate for penumbral imaging), the equation $P_s = N_s$ gives the cutoff frequency k_c :

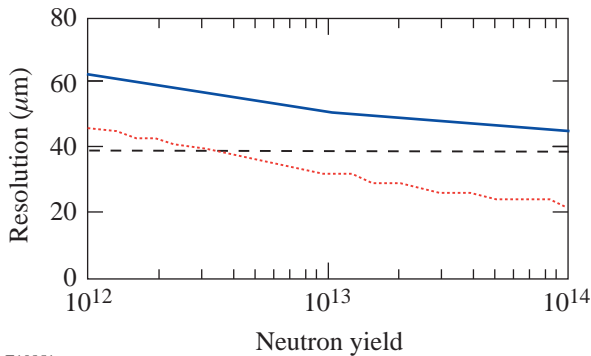
$$k_c = \frac{1}{\pi} \sqrt[6]{\frac{\epsilon N G^2}{4\pi(L_i + L_0)} \frac{(1 - \tau)^2}{\left[(1 - \tau) R_d^2 + \tau (R_d + R_s)^2 \right]} \frac{R_d}{\pi R_s^3}}. \quad (1)$$

The spatial spectrum of the signal beyond the cutoff frequency is within one standard deviation of the noise. Recovering signal information beyond k_c requires sophisticated filtering.¹² In our design, $1/k_c$ is used as a preliminary estimation of the limit of spatial resolution due to the signal-to-noise ratio and the unfolding process.

Combining the effects of statistics on resolution, the shape of the aperture, the pixel size, and the recoil proton range leads to an estimation of the overall spatial resolution δ_s :

$$\delta_s = \sqrt{\frac{1}{k_c^2} + \delta_{\text{bic}}^2 + \left(\frac{2\delta_{\text{pix}}}{G}\right)^2 + \left(\frac{\delta_{\text{rec}}}{G}\right)^2}. \quad (2)$$

Figure 86.33 shows the variation of the overall spatial resolution for neutron yield between 10^{12} and 10^{14} and for a neutron source size of $50\text{-}\mu\text{m}$ diameter. For a high-yield shot, the spatial resolution is $45\ \mu\text{m}$, dominated by the sampling limit ($30\ \mu\text{m}$) and the PSF of the aperture ($24\ \mu\text{m}$) (dotted curve of Fig. 86.33). The design is unable to resolve spatial variation of such a source because the resolution and the source size are comparable. A neutron source size of $100\text{-}\mu\text{m}$ diameter, however, can be differentiated from one of $50\ \mu\text{m}$.



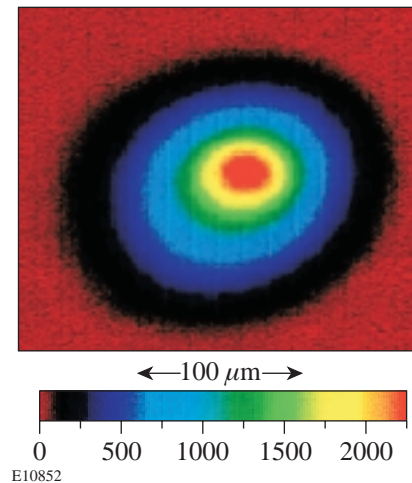
E10851
 Figure 86.33
 The instrument’s contributions to the spatial resolution versus the neutron yield; overall resolution (solid), spatial resolution limit due to the cutoff frequency k_c (dashed) for a $50\text{-}\mu\text{m}$ -diam neutron source, and spatial resolution limit (dotted).

Correct alignment is crucial to the experiment. A straight reference line is established between a $400\text{-}\mu\text{m}$ -diam, back-lighted sphere at target chamber center and an autocollimator near the detector. The penumbral aperture axis is made colinear to an accuracy of $0.1\ \text{mrad}$ using an attached, prealigned half reflecting plate. The aperture is then centered on the back-

lighted sphere to an accuracy of $50\ \mu\text{m}$. The alignment procedure takes at least 2 h for a trained experimentalist to complete.

Several operations are conducted on the raw penumbral image before it is unfolded. First, the average of the CCD backgrounds before and after the shot is subtracted. Then CCD pixels in which neutrons or gamma rays have interacted directly are detected by amplitude discrimination and replaced by the average value of the neighboring pixels. This eliminates CCD pixels that have values more than three times higher than the standard variation of the local average signal; however, CCD pixels where neutrons or gamma rays have created comparable or lower levels than the signal coming from the scintillator still remain. Several shots are also acquired without the aperture. The average of these images is used to correct the image for the spatial variation of the response of the detector and the recording system.

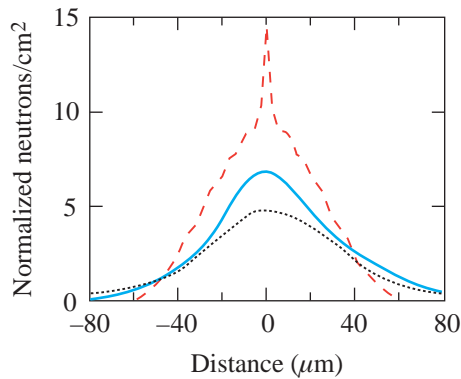
Figure 86.34 shows an unfolded image; Figs. 86.35 and 86.36 show the profiles obtained from the implosions (shots 21054 and 20290) of two glass microballoons filled with 20 atm of DT driven by 1-ns square laser pulses. The shells had thicknesses of $4.2\ \mu\text{m}$ and $2.5\ \mu\text{m}$, diameters of $890\ \mu\text{m}$ and $920\ \mu\text{m}$, and laser energies of 23.1 kJ and 31.1 kJ; they produced yields of 3.6 and 6×10^{13} neutrons, with measured ion temperatures of 10.3 and $\sim 9\ \text{keV}$. The FWHM of the measured neutron source sizes is $62\ \mu\text{m}$ (21054) and $78\ \mu\text{m}$ (20290), respectively. The filter processing limits the minimum detail that can be resolved to $45\ \mu\text{m}$ for shot 21054 and



E10852
 Figure 86.34
 Unfolded image of shot 21054 showing a slight asymmetry.

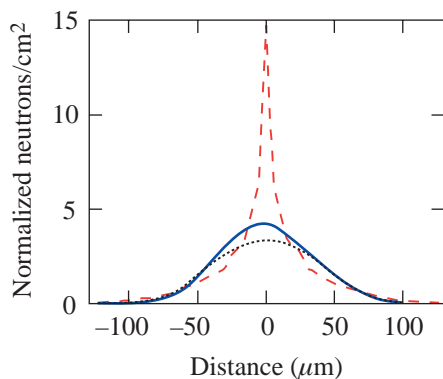
53 μm for shot 20290. These values are in agreement with the expected performance calculated with Eq. (2) (see Fig. 86.33). For comparable neutron yield, the diagnostic resolution performance is better when the source size is smaller, as predicted by Eq. (1).

One-dimensional calculations of these implosions with a radiation-hydrodynamic code¹⁵ were postprocessed using a neutron transport code to produce the calculated neutron image profiles shown in Figs. 86.35 and 86.36. These images were then processed to include the effects of noise by first calculat-



E10853

Figure 86.35
Horizontal lineout (solid) of a DT capsule with a 4.2- μm -thick glass shell (shot 21054) compared to calculated profiles without (dashed) and with (dotted) the effects of experimental noise.



E10854

Figure 86.36
Horizontal lineout (solid) of a DT capsule with a 2.5- μm -thick SiO_2 glass shell (shot 20290) compared to calculated profiles without (dashed) and with (dotted) the effects of experimental noise.

ing a simulated penumbral image, then adding Poisson noise at the level seen in the experiments, and finally deconvolving and smoothing using the same process as used for the data. The resulting profiles in both cases are within the experimental resolution of the observed profiles (all profiles are normalized in 2-D to the same integral). The implosion of the capsule with a 4.2- μm -thick wall had a calculated convergence ratio (initial fuel radius/final fuel radius) of 9, producing the smaller source. The implosion of the capsule with a 2- μm -thick wall was very similar to that of Ress *et al.*⁴ (capsule with a 2- μm wall, 1000- μm diameter, 25 atm DT, 20-kJ laser energy, 1-ns square pulse, convergence ratio of <3 , neutron yield of $\sim 10^{13}$, and a 9-keV ion temperature). Both capsules were calculated to produce an image with a strong central peak. We find that the inclusion of instrumental resolution, which Ress *et al.*⁴ did not address, explains the lack of an observed peak in our data. Our smaller observed FWHM of 78 μm compared to their 150 μm reflects the higher resolution of our imaging system as well as the better irradiation symmetry of OMEGA's 60 beams compared to Nova's 10 beams.

ACKNOWLEDGMENT

We would like to acknowledge the assistance of the OMEGA laser team in executing these experiments, and General Atomics and Los Alamos National Laboratory for fabricating and filling the DT capsules. These experiments were carried out in collaboration and participation of many people, including R. Fisher at General Atomics; S. Chiche, Ph. Millier, C. Ducrocq, C. Labbe, R. Debure, M. C. Monteil, B. Canaud, X. Fortin, and N. Dague at Bruyères le Châtel; S. J. Loucks, J. Mathers, G. Pien, J. Armstrong, and D. D. Meyerhofer at LLE; G. Morgan, F. Cverna, J. Faulkner, M. Wilke, T. Murphy, and C. Barnes at Los Alamos; R. A. Lerche, C. Sangster, and M. Cable at Lawrence Livermore National Laboratory. This work was funded by the Commissariat à l'Énergie Atomique, France, and the US Department of Energy.

REFERENCES

1. J. Paisner *et al.*, *Laser Focus World* **30**, 75 (1994).
2. P. A. Holstein *et al.*, *Laser Part. Beams* **17**, 403 (1999).
3. S. M. Pollaine *et al.*, *Phys. Plasmas* **8**, 2357 (2001).
4. D. Ress *et al.*, *Science* **241**, 956 (1988).
5. O. Delage *et al.*, *Rev. Sci. Instrum.* **66**, 1205 (1995).
6. G. L. Morgan *et al.*, *Rev. Sci. Instrum.* **72**, 865 (2001).
7. J. P. Garçonnet *et al.*, *Laser Part. Beams* **12**, 563 (1994); R. A. Lerche *et al.*, *Laser Part. Beams* **9**, 99 (1991).
8. R. K. Fisher *et al.*, *Rev. Sci. Instrum.* **72**, 796 (2001).

9. J. Birks and D. Fry, *Theory and Practice of Scintillation Counting*, International Series of Monographs in Electronics Instrumentation, Vol. 27 (Pergamon Press, New York, 1964).
10. G. Mosinski and B. Roy, CEA Bruyères le Châtel, Report No. 79/DR 83 (1983).
11. K. A. Nugent and B. Luther-Davies, *Opt. Commun.* **49**, 393 (1984).
12. A. Rouyer, "Unfolding Neutron Penumbral Images Using an Autocorrelation Technique," submitted to *Physical Review Letters*.
13. J. S. Beis, A. Celler, and J. S. Barney, *IEEE Trans. Nucl. Sci.* **42**, 2250 (1995).
14. J. W. Goodman and J. F. Belsher, in *Imaging Through the Atmosphere*, edited by J. C. Wyant (SPIE, Bellingham, WA, 1976), Vol. 75, pp. 141–154.
15. G. B. Zimmerman and W. L. Kruer, *Comments Plasma Phys. Control. Fusion* **2**, 51 (1975).